Solar RRL

RESEARCH ARTICLE OPEN ACCESS

Revealing the Energy Level and Charge Dynamics Interplay in Mixed Pb-Sn Perovskite Solar Cells with Novel Phenoxazine and Phenothiazine Self-Assembled Monolayers

Daniele T. Cuzzupè[1] | Marius Franckevičius[2] | Orestis Karalis[3] | Yekitwork Abebe Temitmie[1,4] | Mantas Marčinskas[5] | Maria Azhar[1] | Neethinathan Johnee Britto[6] | Timo Eberle[7] | Denis Andrienko[6] | Vytautas Getautis[5] | Tadas Malinauskas[5] | Hannes Hempel[3] | Lukas Schmidt-Mende[1]

[1]Department of Physics, University of Konstanz, Konstanz, Germany | [2]Center for Physical Sciences and Technology, Vilnius, Lithuania | [3]Helmholtz-Zentrum Berlin für Materialien und Energie GmbH, Berlin, Germany | [4]Department of Physics, University of Bahir Dar, Bahir Dar, Ethiopia | [5]Department of Organic Chemistry, Kaunas University of Technology, Kaunas, Lithuania | [6]Max Planck Institute for Polymer Research, Mainz, Germany | [7]Institute for Photovoltaics, University of Stuttgart, Stuttgart, Germany

Correspondence: Lukas Schmidt-Mende (lukas.schmidt-mende@uni-konstanz.de)

Received: 22 September 2025 | **Revised:** 11 November 2025 | **Accepted:** 24 November 2025

Keywords: hole-transporting materials | narrow-bandgap perovskite | perovskite solar cells | self-assembled monolayers

ABSTRACT

Hole-selective self-assembled monolayers (SAMs) based on carbazole head groups have enabled major performance improvements of perovskite solar cells (PSCs) by eliminating parasitic absorption and nonradiative losses. However, the energy levels of the carbazole-based, commercially available SAMs poorly match the valence band maximum (VBM) of narrow-bandgap, lead-tin (Pb-Sn) perovskites, relevant for tandem applications. In this work, we expand the library of SAMs compatible with Pb-Sn PSCs by synthesizing four novel SAMs containing phenoxazine (POz) and phenothiazine (PTz) as their head groups and investigate their interaction with the Pb-Sn perovskite in detail. We obtain working devices with all SAMs, but despite significant differences between the highest occupied molecular orbital (HOMO) levels of the SAMs, the open-circuit voltage (V_{OC}) and fill factor (FF) across devices remains similar, suggesting that the role of energy level alignment is less relevant at this interface. Through in-depth analysis including photoluminescence quantum yield (PLQY), transient photocurrent (TPC), and combined time-resolved surface photovoltage (trSPV) and time-resolved photoluminescence (trPL) measurements, we unveil the charge extraction dynamics of these systems featuring different head groups and HOMOs. This work highlights that the SAMs' structure affects the overall charge extraction process and provides insights into the strategies needed to maximize charge extraction for more efficient PSCs.

1 | Introduction

Since their first introduction in solar cells in 2009, metal halide perovskites have gained enormous attention in the solar cell community due to their excellent optoelectronic properties such as high absorption coefficients, tunable bandgaps, and low manufacturing cost. These properties could enable power conversion efficiency (PCE) values up to 26.7% for single-junction devices on a lab scale, thereby offering a compelling perspective for commercialization [1–7]. Highly efficient single-junction perovskite solar cells (PSC) typically use lead (Pb) iodide perovskite compositions as their absorbers, resulting in bandgaps in the range of 1.5–1.8 eV [8–10]. As the Shockley–Queisser efficiency limit for a single-junction on a lab scale is being approached, the tandem solar cell (TSC) concept, which allows reducing thermalization losses and therefore enabling higher efficiencies, is gaining increasing attraction [11, 12]. While to date the most efficient silicon (Si)-perovskite tandems reach PCEs up to 34.2%, the Si part retains the issues typical of this material, such as the high purification costs [7, 13]. All-perovskite tandems consisting of one narrow-bandgap (NBG)

and one wide-bandgap (WBG) perovskite absorber could offer a valuable alternative [14, 15]. Compared to Si-containing devices, all-perovskite tandems are also compatible with the fabrication of flexible solar cells, due to the pliable nature of perovskite materials [16]. In NBG perovskite compositions, a substantial part of Pb is typically replaced with tin (Sn). The alloying of these two metals within the perovskite results in bandgaps in the range of 1.2–1.3 eV, which are narrower than both pristine counterparts due to the so-called bandgap bowing effect [17, 18]. Many of the latest advances in PSC were made possible by the use of hole-transporting self-assembled monolayers (SAMs), allowing fast and effective hole collection, thereby limiting interfacial recombination losses [19–21]. Over the past decade, several tens of phosphonic acid-based, hole-transporting SAMs have been introduced and successfully implemented in p-i-n PSCs. For details, we refer the reader to some recent and comprehensive review articles on the topic [22–25]. The most prominent, commercially available SAMs such as 2PACz, 4PACz, and Me-4PACz have highest occupied molecular orbital (HOMO) levels in the range of 5.5–5.8 eV and as such they align well with the valence band maxima (VBM) of Pb perovskites [26]. However, the same might not hold true for Sn-containing perovskites, which have been reported to have a shallower edge around 5.2–5.3 eV [27, 28]. In this work, we designed and synthesized four novel SAMs based on the phenoxazine (POz) and phenothiazine (PTz) head groups to expand the library of the available SAMs and to understand the interplay between HOMO of the SAMs and VBM of the perovskites. Our results outline a complex dynamic between charge extraction and interfacial recombination and stress the need of substantial improvements in the severely limiting perovskite/electron-transport material (ETM) interfaces, which constitute the charge collection bottleneck of the state-of-the-art PSCs.

2 | Results and Discussion

2.1 | Energy Levels Alignment and Solar Cell Performance

In order to understand to what extent the energy level alignment between the valence band maximum (VBM) of the Pb-Sn perovskite and the HOMO of the hole-transport layer (HTL) determines the effective hole collection and ultimately the device efficiency, we initially measure the VBM of the neat -Pb-Sn perovskite film using photoelectron spectroscopy in air (PESA), confirming the reported values of 5.2–5.3 eV (Figure S1, Supporting Information) [29–31]. Here, it is important to specify that the values obtained by standard photoelectron spectroscopic measurements, including ultraviolet photoelectron spectroscopy (UPS) and PESA, only provide an approximate value that it is subject to change when the material is incorporated into a multilayered device [32, 33]. Since the energetics of the buried HTL/perovskite is difficult to access directly via the usual material characterization techniques, one alternative is testing empirically the charge collection efficiency when solar cells are fabricated using the Pb-Sn perovskite absorber in combination with HTLs having either shallower, approximately equal, or deeper HOMO levels than the approximate VBM of the absorber. Therefore, we synthesized the adducts 2PAPOz, 2PAPTz, 4PAPOz, and 4PAPTz

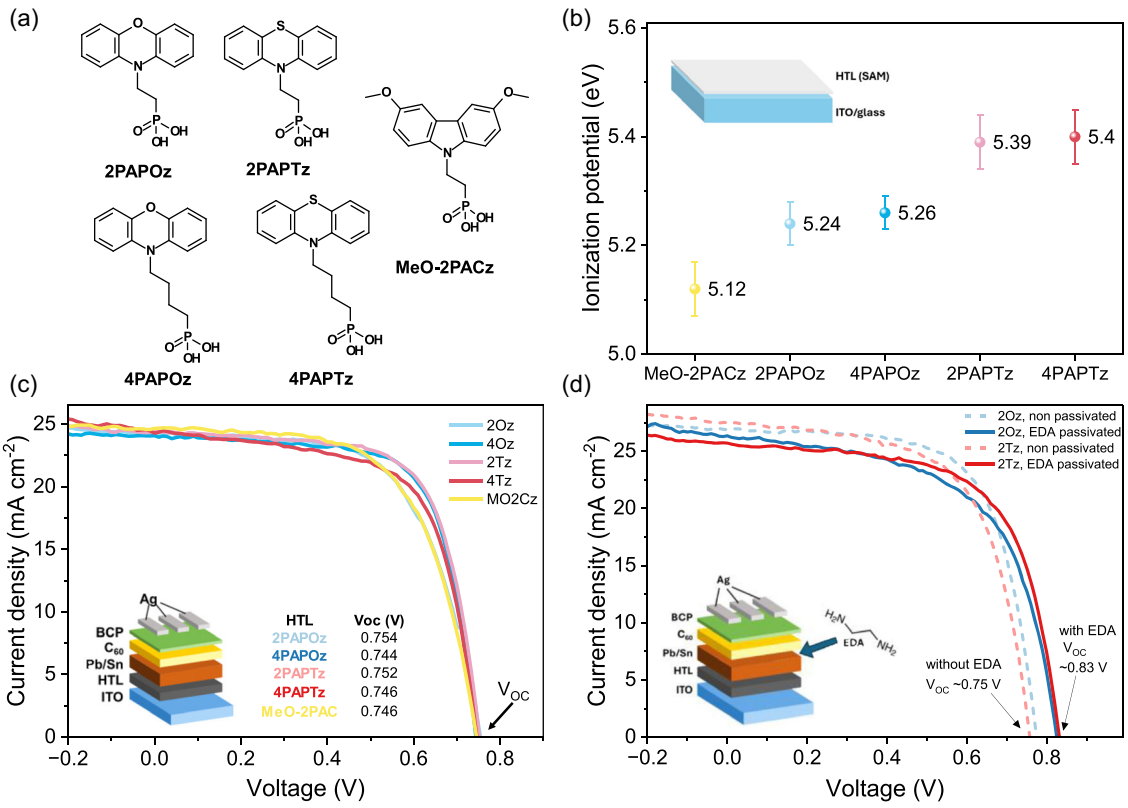

FIGURE 1 | (a) Molecular structure of the SAMs used in this work. (b) Ionization potential of the SAMs as measured by PESA (inset: scheme of the sample). (c) Representative *J–V* curves of solar cells using the five different HTLs (inset: device architecture and V_{OC} values. (d) Representative *J–V* curves of solar cells using 2PAPOz and 2PAPTz as their HTL, nonpassivated or EDA-passivated, respectively (inset: device architecture and passivation scheme).

and compared them to the commercially available MeO-2PACz. The synthesis and the characterization of the four new SAMs is described in detail in the Supporting Information. These adducts (Figure 1a) are inspired to the widely used SAMs featuring a head group containing a carbazole system (Cz), an aliphatic chain (C_2-C_6), and a phosphonic acid (PA) anchoring group, as in MeO-2PACz. In our approach, we replaced the carbazole head groups with phenoxazine (POz) or phenothiazine (PTz), using either a two- or four-membered aliphatic chain and keeping the phosphonic acid anchoring group. Bromine-substituted POz- and PTz-based SAMs have been reported in recent literature [34, 35], however in our approach we did not include any substituents on the POz and PTz head groups. Using PESA, we measured the energetics of all SAMs deposited on ITO substrates, which confirmed that the commercial MeO-2PACz has a HOMO level of ∼5.1 eV, slightly shallower than the VBM of the perovskite, the phenoxazine-based SAMs' HOMOs of ∼5.2 eV are circa equal to the VBM perovskite, while the phenothiazine-based SAMs' HOMOs of ∼5.4 eV are 200 meV deeper than the approximate VBM of the perovskite (Figure 1b).

To elucidate the correlation between the molecular structure of SAMs and the variations in their VBM levels, we performed density functional theory (DFT) calculations (see Supporting Information for computational details). The optimized molecular structures of the SAMs are presented in Figure S2 (Supporting Information), along with their corresponding HOMO and lowest unoccupied molecular orbital (LUMO) plots and energy levels. The LUMOs are primarily delocalized over the π-conjugated rings, with negligible electron density observed on the oxygen or sulfur atoms within the heterocyclic bridge. In contrast, the HOMOs are predominantly localized on the phenoxazine and phenothiazine heads, with significant electron density on the heteroatoms. In all five SAMs, neither the linkers nor the tail groups exhibit notable contributions to either the HOMO or LUMO, suggesting their minimal influence on the electronic structure. Using Koopmans' theorem, we approximated the ionization energies as the negative of the HOMO energies. The higher ionization energies of the phenothiazine- and phenoxazine-based SAMs can be rationalized by the electron-withdrawing character of the oxygen and sulfur heteroatoms, which stabilize the HOMO and increase the energetic cost of electron removal. In contrast, MeO-2PACz features a strongly electron-donating methoxy group that increases the electron density on the aromatic system, thereby destabilizing the HOMO and reducing its ionization energy. To further validate this interpretation, vertical ionization energies were computed and compared with PESA measurements (see Figure 1b and Figure S3, Supporting Information). The calculated values show good consistency with the experimental data substantiating that the different functional groups on the SAMs modulate their geometry and their properties. Clearly the phenothiazine-based SAMs exhibit higher ionization energies than their phenoxazine analogs, whereas the commercial MeO-2PACz SAM displays the lowest ionization energy among all the systems studied, which further affirms the results calculated according to Koopman's theorem.

We then proceeded to fabricate solar cell devices with the architecture ITO/HTL/Pb-Sn perovskite/C_{60}/BCP/Ag, as depicted in the inset of. Figure 1c, which displays typical *J*–*V* curves for devices employing each of the five studied HTLs. Intriguingly, despite the energetic differences among the HTLs' HOMOs, spanning a range of 300 meV, the open-circuit voltage (V_{OC}) remains similar across all systems at around 0.75 V.

Obviously, the V_{OC} is influenced by both the hole collection at the perovskite/HTL interface and the electron collection at the perovskite/electron-transport layer (ETL) interface. Therefore, if the latter is suboptimal due to surface or interfacial defects [36, 37], it may result in a bottleneck for the V_{OC}, thus making the energy level alignment at the hole-selective interface less relevant. For this reason, we employed the well-known surface passivation treatment with ethylenediamine (EDA), which has been reported as a facile strategy compatible with and beneficial to many perovskite compositions, including neat-Pb triple cation and WBG perovskites and neat-Sn perovskites [38–42]. Figure 1d shows four representative *J*–*V* curves for devices containing 2PAPOz and 2PAPTz as their HTL, nonpassivated and EDA-passivated, respectively. Even though the EDA passivation results in improved V_{OC} (at around 0.83 V) and overall PCE for both HTLs (results over many devices in Figures S4 and S5), the magnitude of the improvement is approximately the same for both systems, suggesting that the perovskite/ETL side might be the bottleneck of the overall charge collection even after passivation. This further highlights the need for the perovskite community to further improve the ETL interface or come up with new strategies, including novel materials and unconventional deposition techniques minimizing the significant losses at this specific interface. The commonly deployed material characterization techniques such as scanning electron microscopy (SEM), X-ray diffraction (XRD), and steady-state photoluminescence (PL) do not reveal significant differences, suggesting that the bulk properties of the perovskite remain unchanged when grown on top of the five different SAMs (Figure S6, Supporting Information).

While the *J*–*V* curves reveal the suitability of all novel SAMs for the fabrication of working Pb-Sn PSCs, a better understanding of the nonradiative losses in the perovskite stacks deposited on different HTLs is necessary. Therefore, we performed photoluminescence quantum yield (PLQY) measurements. As depicted in Figure 2a, the Pb-Sn perovskite films deposited on quartz glass resulted in the highest PLQY, followed by MeO-2PACz, the phenoxazine-containing HTLs 2PAPOz and 4PAPOz, and then by the phenothiazine-containing HTLs 2PAPTz and 4PAPTz. Finally, when a thin C_{60} layer was evaporated on top of the perovskite, the resulting PLQY amounted to merely half of the quartz glass case, once again highlighting the high losses at this interface.

2.2 | Assessment of Charge Carrier Extraction

For a more in-depth analysis, we performed combined time-resolved photoluminescence (trPL) and time-resolved surface photovoltage (trSPV) experiments. Notoriously, standard trPL measurements are difficult to interpret. The challenge arises from the co-occurrence of two main phenomena: (i) nonradiative recombination and (ii) charge carrier extraction into the charge-selective layer, the former being detrimental and the latter beneficial for the sake of solar cell efficiency. However, both result in the quenching of the observable PL signal [43]. On the other hand, trSPV allows for the direct probing of the fast charge transfer, further enabling the extent and the timescale of the charge transfer by inspecting the amplitude and the rate of the transient SPV signal. Thus, performing these measurements sequentially

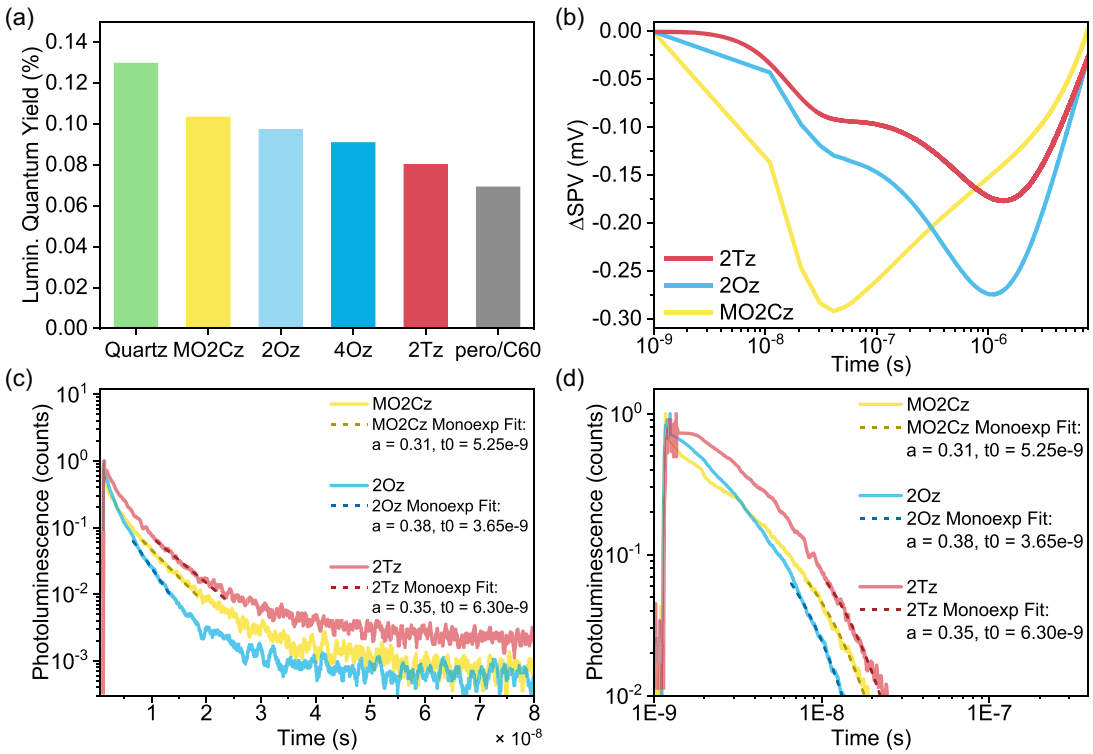

FIGURE 2 | (a) Luminescence quantum yields values for Pb-Sn perovskite deposited on quartz glass, on the different SAMs and for a perovskite/C_{60} stack. (b) trSPV measurement performed on the Pb-Sn perovskite deposited on three different SAMs. (c) Semilogarithmic trPL plots of the same samples of (b); the monoexponential decay fitting functions are shown with a dashed line. (d) Logarithmic trPL plots of the same samples with the same fitting functions shown.

on the same sample is essential to disentangle concurring phenomena. The SPV transients in Figure 2b start from an amplitude of 0, as we subtracted the photovoltage before the arrival of the laser pulse (i.e., the photovoltage from previous laser pulses and ambient light). Hence, we refer to the *y*-axis as "ΔSPV" rather than "SPV." All samples exhibit a negative SPV signal after the first 10 ns. It is important to note that the resolution is limited to 10 ns. Some other transients, measured with higher resolution, showed an initial positive signal within the first 10 ns. However, for 2PAPOz, no higher resolution transient is available, so all data are presented with the 10 ns resolution. The early positive signal is most likely associated with the initial charging of the samples, as the newly formed holes first migrate toward the already positively charged surface. The negative SPV indicates an excess of negative charge on the surface of the sample, resulting from holes moving toward the HTL. For MeO-2PACz, this charge extraction process occurs more rapidly than in the other samples, with the SPV peaking at 40 ns. Subsequently, the signal decays to zero as the holes are injected back into the bulk and recombine there. The other samples exhibit a shoulder around the same timescale (∼40 ns), which may indicate a similar process as observed in MeO-2PACz. However, the negative SPV signal in these samples becomes more pronounced, forming a second shoulder, which suggests an additional, more dominant process. MeO-2PACz demonstrates a faster increase in the SPV signal and reaches a higher amplitude compared to 2PAPOz and 2PAPTz. This indicates faster charge extraction and greater charge separation in MeO-2PACz.

TrPL was captured up to 80 ns, during which it decayed by approximately three orders of magnitude. The semilogarithmic plot in Figure 2c reveals a multiexponential decay, as indicated by the nonconstant slope and the progressively slower decay over time. We fitted the data with a monoexponential decay between 0.1 and 0.01 of the maximum amplitude, as also depicted in Figure 2d. All samples exhibit similar trPL decay times in the order of a few nanoseconds, with 2PAPOz decaying slightly faster at 3.7 ns, followed by MeO-2PACz at 5.3 ns, and 2PAPTz at 6.3 ns. These decay times are considerably shorter than those for lead-based halide perovskites but relatively long if compared to pure Sn perovskites such as FASnI3, for which we previously reported a decay time of 0.5 ns [44].

Comparing the trPL with the trSPV shows that trPL quenches during the initial hole extraction process, within the first ∼10 ns. Subsequently, it appears that no significant PL occurs, indicating the absence of remaining holes in the perovskite. We attribute this initial extraction process to the separation of electrons and holes in the perovskite layer, and possibly to hole transfer within the headgroup of the SAMs. The later hole extraction process, which is more pronounced in 2PAPOz and 2PAPTz, may be attributed to tunneling through the backbone of the SAM molecules, which has been shown to limit the charge extraction rate through the SAMs [43].

These results suggest that MeO-2PACz facilitates faster hole transfer (as indicated by the quicker SPV peak) and extracts more holes (as evidenced by the larger SPV amplitude) than the other SAMs. Consequently, MeO-2PACz appears to have superior HTL properties, but no significant difference is observed when comparing the photovoltaic performance parameters averaged over a large number of devices (Figures S4 and S5), resulting in comparable or slightly higher V_{OC} values for 2PAPOz and 2PAPTz over

MeO-2PACz, and comparable or slightly higher PCE values for 2PAPOz over MeO-2PACz.

Next, we examine the voltage-dependent trPL measurements of PSCs comprising different SAMs. We measured the trPL decays up to 50 ns, by varying the applied pulsed voltage from 0 to 1.8 V. For each of the plots in Figure 3, we can separately assess the fast and the slow decay components and their lifetime dependences on the voltage. When the field is not applied or is screened, the trPL decay predominantly represents the recombination of charge carriers, as well as their extraction process when the charge carriers diffuse towards interfaces, due to the built-in electric field.

In contrast, the application of the voltage to the devices could modify the internal built-in field, resulting in drift transport of the charge carriers, which can reduce recombination at the interfaces increasing carrier injection. Considering that the used perovskites and their contacts with the ETM are identical in all samples, the differences in trPL decays are primarily determined by the interface quality of the SAMs. If the carrier recombination at the interfaces is low and carrier movement is not impeded by the barriers, the injection of charge cariers at the interface should not depend significantly on the applied external electric field. In devices containing 2PAPOz and 4PAPOz as their HTL, the fast PL decay component accelerates with increasing voltage, suggesting that the additional applied electric field is required to enhance carrier extraction, which we do not see for the 2PAPTz and commercial MeO-2PACz counterparts. The acceleration of the PL decay with increasing applied voltage indicates that the presence of energy states at the SAM/perovskite interface impedes hole transfer toward SAM, requiring additional electric field to overcome their activation. While the absence of trPL acceleration with applied voltage, suggests that the electric field is either screened by photogenerated carriers [45] or that hole transfer toward SAM is fast enough to respond to field induced energy level shifts at interface [46]. The latter is more likely, as the low carrier injection levels in our experiments (<100 nJ cm^{-2}) make electric field screening less important. Moreover, screening by electric field induced ion migration should be also ruled out, as the applied 2 µs voltage pulses with a low repetition rate of 10 kHz, allow the system to relax for hundreds of microseconds between pulses.

The slow PL decay components remain unaffected by change in voltage in the 2PAPOz, 4PAPOz, and MeO-2PACz devices. We attribute this observation to intrinsic properties or defect states within the material that do not respond to the electric field. In contrast, for the 2PAPTz-based device, the slow PL decay component becomes slower with increasing voltage. This is in contrast to all other samples and could be due to an increase in the population of trapped carriers caused by the applied electric field to these devices. This results in a longer release time for the trapped charge carriers.

We also investigated the transient photoresponse of the samples in a lateral geometry using interdigitated combs of Pt electrodes (IDE) with a 5 µm interelectrode spacing. The IDEs were coated with SAMs, followed by the deposition of perovskite films on top (Figure 4a). In this configuration, the SAMs were deposited on a glass/Pt substrate instead of glass/ITO. However, since the spin-coating process was performed identically for both substrates and typically results in a thin stacked layer rather than an ideal monolayer, we do not expect significant differences in the behavior of the SAMs on the two surfaces. The samples were excited with short laser pulses under an applied external electric field. The photocurrent decay of the samples results from the decrease in charge carrier concentration, which is determined by their transition towards interfaces, recombination, or trapping at defects.

The photocurrent kinetics of all samples are presented in Figure 4b–e, revealing a triexponential decay behavior. The decay shows a very fast component lasting for less than 10 ns, an intermediate component around 100 ns, and a slow decay component persisting over several microseconds. Notably, all samples show very similar lifetimes, with only slight variations in amplitudes, especially for sample 4PAPOz. These differences might be

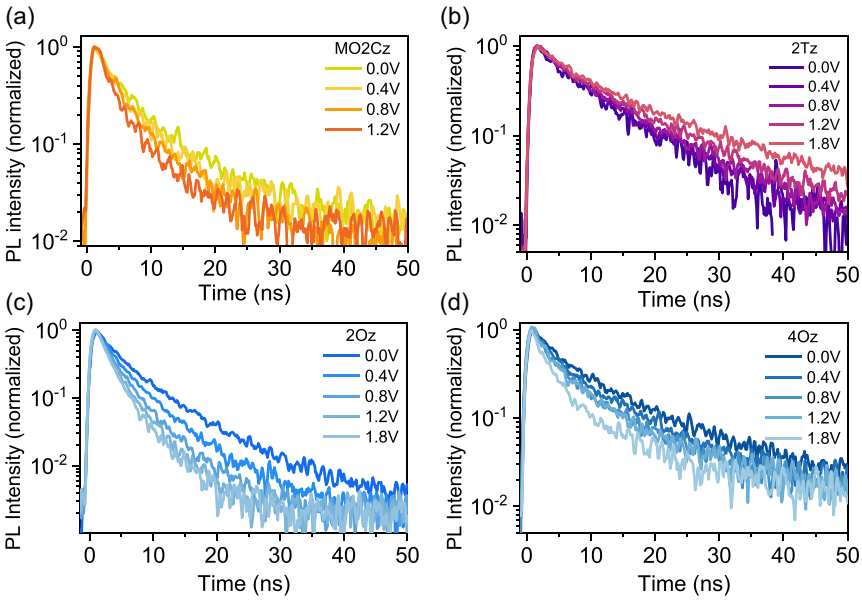

FIGURE 3 | Voltage-dependent trPL measurements performed on full solar cell devices featuring (a) MeO-2PACz, (b) the phenothiazine-based 2PAPTz, and (c,d) the phenoxazine-based 2PAPOz and 4PAPOz self-assembled monolayers as their HTLs.

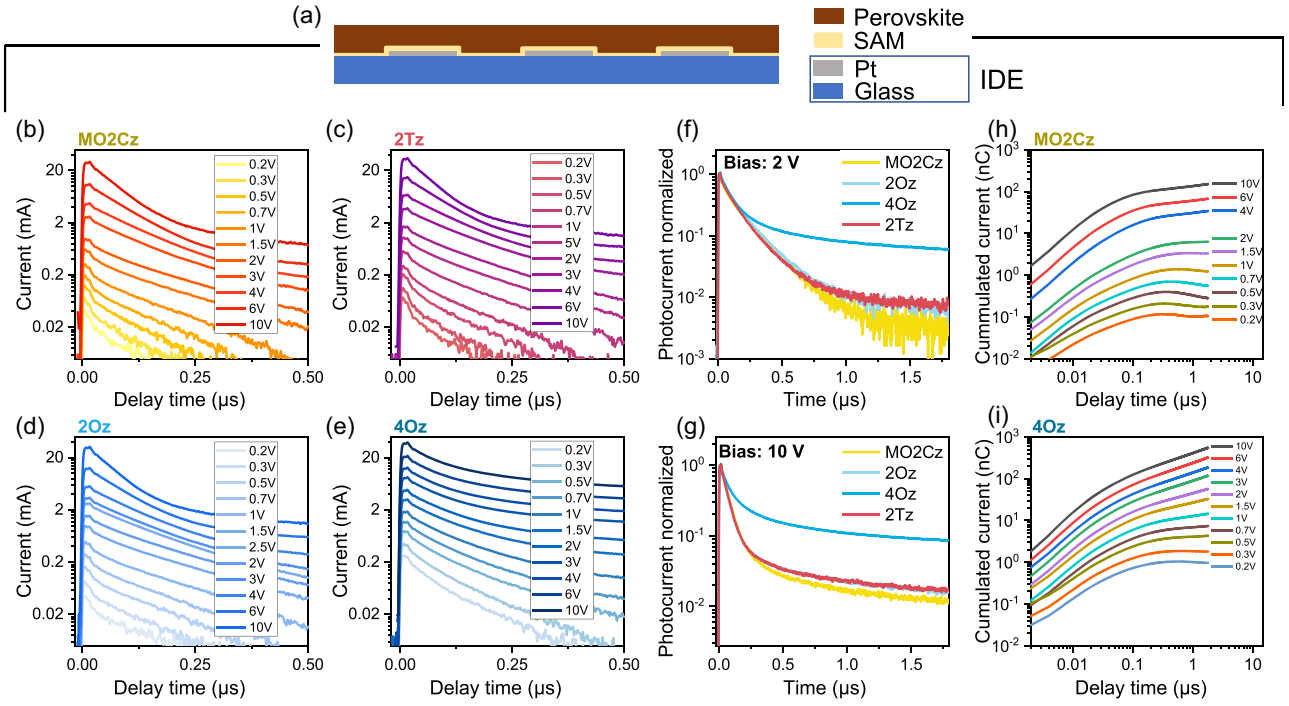

FIGURE 4 | (a) Scheme of the interdigitated electrodes used for all experiments whose result are in the rest of the figure. (b–e) Transient photocurrent plot as a function of the applied voltage bias. (f,g) Comparison of different HTLs at an applied bias of 2 and 10 V. (h,i) Cumulated charge collection resulting from the corresponding transients for MeO-2PACz and 4PAPOz, respectively.

influenced by SAMs. After initial carrier generation, the carriers rapidly undergo relaxation, where the initial fast decay component might be attributed to electron trapping [43], occurring more rapidly than hole extraction, which is represented as the intermediate decay component. The fast decay component is more pronounced at low applied voltages, when the applied electric field across the perovskite is weak. While increasing the voltage accelerates the transport of holes by driving them more efficiently toward the corresponding electrode. This results in a reduced contribution of the fast electron trapping-related decay component. At higher voltages, the photocurrent becomes more dominated by the extraction of holes. This also well agrees with the slow decay component, which could be attributed to the extraction of trapped electrons at higher voltages.

The voltage dependence of the slow decay component is complex. At low voltages, its contribution becomes negative, but further increasing the voltage its contribution becomes positive and at high voltages it slows down. The negative component is evidently related to the screening of the built-in field created either by mobile ions, accumulated electrons, or a combination of both [47]. At low applied electric fields, electrons can move toward positive electrode, where they may be trapped or accumulated at the SAM/perovskite interface due to an energetic barrier, creating a localized region of negative charge near the positive contact. Meanwhile, slowly moving mobile ions can create a positive charge region near the opposite electrode. These conditions create an internal electric field with opposite polarity to the applied field, resulting in a negative net current when a low voltage is applied.

As the applied voltage increases, the stronger external applied electric field overcomes the opposing internal field, resulting in the release of trapped carriers and more efficient charge carrier extraction. When comparing normalized transient photocurrent (TPC) kinetics presented in Figure 4f,g, the slow decay component for the samples containing 2PAPOz, MeO-2PACz, and 2PAPTz SAMs shows a very similar behavior, whereas the amplitude of the 4PAPOz device is significantly increased. The integrated TPC decay (Figure 4h,i) representing the cumulated current (total extracted charge), shows that all samples have a similarly fast initial carrier extraction component attributed to hole extraction. However, an additional slow component for 2PAPOz, MeO-2PACz, and 2PAPTz SAMs almost saturates at higher voltages, while it further increases for samples with 4PAPOz molecules. The persistent increase in the slow component additionally suggests the presence of carriers that are gradually extracted from the perovskite. This further confirms that films with 4PAPOz molecules have more trapped electrons than other samples. Since the perovskite composition is identical in all films, the charge carrier trapping probably occurs at the SAM/perovskite interface.

3 | Conclusions

In conclusion, this study expands the available library of SAMs available for PSCs, showing that all examined SAMs yield working devices based on NBG Pb-Sn perovskite. Despite the HOMO levels—computationally determined and experimentally verified—of the investigated SAMs aligning differently with the VBM of the Pb-Sn perovskite, the influence of this alignment on device performance was found to be secondary in these systems, as reflected in consistent V_{OC} and fill factor (FF) values across devices, for both nonpassivated and EDA-passivated perovskite surfaces. These results strongly suggest that in these systems, the perovskite/C_{60} interface is a predominant limiting factor that hinders

the charge carrier extraction. The in-depth analysis of charge extraction in cells and half-cells containing carbazole-, phenoxazine-, and phenothiazine-based SAMs illustrates the complex dynamics between extraction and recombination. TrPL and trSPV studies reveal differences in fast hole transfer and interfacial recombination dependent on the SAM structures, outlining similarities between POz and PTz-based SAMs, and differences between these latter and MeO-2PACz. Voltage-dependent trPL reveals the presence of possibly limiting energy states for 2PAPOz and 4PAPOz, which are absent in 2PAPTz or MeO-2PACz. The TPC analysis suggests the presence of trap states for 4PAPOz, which can be attributed to the longer aliphatic chain. The molecular design of HTLs for Pb-Sn PSCs remains relevant, and the tunability of the SAMs' energy levels via their head group is a valuable strategy to boost hole extraction. We point out that while hole-transporting SAMs are close to optimal for hole extraction, further improvements at the perovskite/ETL interface remain crucial for both the device optimization and the better understanding of the complex interplay between simultaneous extraction of electrons and holes, recombination and interfacial phenomena.

4 | Materials and Methods

4.1 | Materials

For the PSCs fabrication, ITO-coated glass substrates were acquired from *Luminescence Technology Corp* (thickness 2 mm, ~15 Ω/□). Formamidinium iodide (>99%), methylammonium iodide (>99.99%) were purchased from *Greatcell Solar*. Lead (II) iodide (99.99% trace metal basis) and MeO-2PACz (>98%) were purchased from *TCI Chemicals*. Tin (II) iodide (>99.9%) was purchased from *Thermo Scientific*. Buckminsterfullerene (C_{60}, >98.5%) and bathocuproine(BCP) (>99.0%) were acquired from *Ossila*. Chlorobenzene (anhydrous, 99.8%), lead (II) thiocyanate, tin (II) fluoride (99%), ethylenediamine (≥99%), diethyl ether (anhydrous, ≥99.7%, containing 1 ppm BHT as inhibitor), isopropyl alcohol (anhydrous, 99.5%) were purchased from *Sigma Aldrich*. Dimethylformamide (99.8%, extra dry) and dimethyl sulfoxide (99.7 + %, extra dry) were purchased from *Acros Organics*. Absolute ethanol was purchased from *VWR*. All chemicals were used without further purification or processing.

4.2 | Synthesis and Chemical Characterization of Novel SAMs

For the synthesis of nPAX ($n = 2,4$; X = POz, PTz), chemicals were purchased from *Sigma Aldrich* and *TCI Europe* and used as received without further purification. ^{1}H NMR spectra were recorded at 4007MHz on a *Bruker Avance III* spectrometer, ^{13}C NMR spectra were collected using the same instrument at 101 MHz. The chemical shifts, expressed in ppm, were relative to tetramethylsilane (TMS). All the NMR experiments were performed at 25°C. Reactions were monitored by thin-layer chromatography on *ALUGRAM SIL G/UV254* plates and developed with UV light. Silica gel (grade 9385, 230–400 mesh, 60 Å, *Sigma Aldrich*) was used for column chromatography. Elemental analysis was performed with an *Exeter Analytical CE-440* elemental analyzer, Model 440 C/H/N/. Electrothermal *A. KRÜSS M3000* capillary melting point apparatus was used for determination of melting points. Details about the synthesis and analysis of the individual adducts are available in the Supporting Information.

4.3 | DFT Calculations

DFT calculations were performed with Gaussian 16 using B3LYP/Def2-SVP and Grimme's D3 correction; full computational details are provided in the Supporting Information.

4.4 | Precursor Solutions

For each SAM, a 0.2 mM solution in ethanol was prepared and stored in a nitrogen atmosphere, which was then used for several batches. The Pb-Sn perovskite precursor solution was prepared by mixing separately prepared $FASnI_3$ and $MAPbI_3$ solutions. The $FASnI_3$ solution was prepared by combining FAI and SnI_2 at a concentration of 1.15 M with the presence of 10% (i.e., 0.115 M) of SnI_2 in DMF:DMSO 4:1. After stirring for several hours, the solution was filtered through a 0.20 μm PTFE filter. The $MAPbI_3$ solution was prepared by combining MAI and PbI_2 at a concentration of 1.15 M with the presence of 3.50 mol% (0.04 M) of $Pb(SCN)_2$ in DMF:DMSO 9:1 and stirring at 70°C for 30 min. Then, the two solutions were combined in a volume ratio of 1.5:1 $FASnI_3$:$MAPbI_3$ to yield the $FA_{0.6}MA_{0.4}Sn_{0.6}Pb_{0.4}I_3$ composition. The passivation solution was prepared by dissolving EDA in isopropyl alcohol at a concentration of 0.90 mM.

4.5 | Perovskite Solar Cell Fabrication

The ITO substrates were cleaned by ultrasonication in soapy water, acetone and isopropyl alcohol for 15 min each, then they were carefully dried and placed in an UV/Ozone cleaner (*Ossila*) The SAMs precursor solutions were spin-coated on top of the substrates in a N_2-filled glovebox at a spin speed of 3000 rpm for 30 s, followed by annealing at 100°C for 10 min each. Afterward, the Pb-Sn perovskite solution was spin-coated onto the HTLs at 4000 rpm for 60 s. At 15 s after the start, a generous amount of diethyl ether was pipetted onto the spinning substrate, followed by annealing at 100°C for 10 min each. The substrates were then transferred into a thermal evaporator (*Oerlikon*), where 25 nm of C_{60} were deposited at a rate of 0.1 Å/s, followed by 7 nm of bathocuproine (0.17Å/s) and finally 100 nm of silver (1 Å/s). All thermal evaporations were carried out under a vacuum $<8 \times 10^{-6}$ mbar.

4.6 | Characterization

PESA was carried out using an *AC-2* system purchased by *Riken Instruments*. Quantity of light correction was performed before starting the measurement. The current density–voltage characteristics curves of the PSCs were recorded under equivalent 1 sun illumination with a step size of 0.05 V and a delay of 0.01 s in a nitrogen filled glovebox with an assembly of a *Keithley 2400 SMU* and a *LOT 300W* Xenon solar simulator, calibrated with a Si reference diode certified from *ISE Fraunhofer*. The PLQY was measured using a *LuQY Pro* setup from *Quantum Yield Berlin* equipped with a 550 nm longpass filter between the

sample and the detector. The raw PL spectra acquired with this instrument were used for the steady-state PL analysis. Scanning electron microscope (SEM) images were acquired with a *Gemini 500 FESEM* system from *Zeiss* equipped with an in-lens detector. The charge carrier extraction and nonradiative recombination losses at the interface between perovskite and HTL were investigated in this work by combining trSPV and trPL, which were performed under identical photogeneration conditions. TrPL is a common technique for measuring charge carrier recombination in semiconductors. TrSPV studies carrier dynamics at buried interfaces and therefore complements trPL by distinguishing charge carrier extraction (appears as the rise of SPV) from recombination (appears as the decay of SPV). Also, the direction of charge carrier movement can be identified from the sign of the voltage [43]. The samples were excited in both experiments with a femtosecond laser (*Menlo BlueCut*) with a wavelength of 515 nm wavelength and repetition rates of 125 kHz. The laser power was attenuated with neutral density filters to 24 pJ cm^{-2} $pulse^{-1}$. This corresponds to a photoexcitation of 6×10^{14} carriers cm^{-3}. This carrier concentration is typical for such perovskite thin films to open-circuit conditions under 1 sun illumination. The SPV signal was measured in the configuration of a parallel plate capacitor. The capacitor is formed between the reference electrode, a quartz cylinder partially coated with SnO2:F (reference electrode) and the sample electrode, which is ITO of the device. The encapsulation on top of the perovskite is the insulator of the capacitor which increases the voltage/signal and no other insulator, e.g., mica-sheet was needed. The signal was measured via a high-impedance buffer by an oscilloscope [48]. The PL emission was measured by time-correlated single photon counting with *PicoHarp300*. To this end, a Geiger-mode avalanche photodiode was used with a 530 nm long-pass filter in front of it to suppress the 515 nm laser light. For voltage-dependent trPL measurements, transient photoluminescence signals were detected using a streak camera system (*Hamamatsu C5680*) operating in single-sweep mode. A femtosecond Yb:KGW oscillator (*Pharos*, *Light Conversion Ltd*) with a frequency doubler (*HIRO*, *Light Conversion Ltd*) producing 515 nm sub-100-fs pulses at a 76 MHz repetition rate was employed, and a pulse picker was used to reduce the repetition rate to 2 kHz in the single-sweep mode for nanosecond timescales. Electrical pulses with duration of 2 µs were applied to the PSCs devices using a *Tektronix AFG3101* function generator. TPC investigations were performed with an *Agilent Technologies DS05054A* oscilloscope using 50 Ω input resistor and a *Tektronix AFG 3101* function generator. Samples were excited by nanosecond Nd:YAG Laser *PL201* (*EKSPLA*) generating 4 ns duration pulses with 200 Hz repetition rate at 532 nm wavelength.

Acknowledgments

D.T.C. gratefully acknowledges funding from the German Federal Ministry for Economic Affairs and Climate Action (BMWK) through the APERO project (ref. no. 03EE1113C), Dr. Azhar Fakharuddin for initiating the cooperation leading to this work and insightful discussions, Dr. Yenal Yalçınkaya for feedback on the manuscript, Clara Würth and Tim Vogel for supporting lab tasks. Y.A.T. acknowledges funding by the International Science Program (ISP/IPPS ETH: 03, 2021-2026) and the German Academic Exchange Service (DAAD). O.K. and H.H. acknowledge funding from the German Research Foundation (DFG) through the SPP2196 project. M.F. acknowledges funding by a grant (agreement No. P-MIP-22-210) from the Research Council of Lithuania. M.M., T.M., and V.G. acknowledge funding from the Science Council of Lithuania and the Ministry of Education, Science and Sports of the Republic of Lithuania from the state budget under the program "University Excellence Initiative" through the project "Technological and Physical Sciences Excellence Centre (TiFEC)" No. S-A-UEI-23-1.

Open Access funding enabled and organized by Projekt DEAL.

Funding

This study was supported by Bundesministerium für Wirtschaft und Klimaschutz (03EE1113C); German Academic Exchange Service (DAAD); Deutsche Forschungsgemeinschaft (SPP2196); Research Council of Lithuania (P-MIP-22-210); Science Council of Lithuania (S-A-UEI-23-1).

Conflicts of Interest

The authors declare no conflicts of interest.

Data Availability Statement

The data that support the findings of this study are available from the corresponding author upon reasonable request.

References

1. A. Kojima, K. Teshima, Y. Shirai, and T. Miyasaka, "Organometal Halide Perovskites as Visible-Light Sensitizers for Photovoltaic Cells," *Journal of the American Chemical Society* 131, no. 17 (2009): 6050–6051, https://doi.org/10.1021/ja809598r.

2. M. M. Lee, J. Teuscher, T. Miyasaka, T. N. Murakami, and H. J. Snaith, "Efficient Hybrid Solar Cells Based on Meso-Superstructured Organometal Halide Perovskites," *Science* 338, no. 6107 (2012): 643–647, https://doi.org/10.1126/science.1228604.

3. S. A. Kulkarni, T. Baikie, P. P. Boix, N. Yantara, N. Mathews, and S. Mhaisalkar, "Band-Gap Tuning of Lead Halide Perovskites Using a Sequential Deposition Process," *Journal of Materials Chemistry A* 2, no. 24 (2014): 9221–9225, https://doi.org/10.1039/c4ta00435c.

4. S. De Wolf, J. Holovsky, S.-J. Moon, et al., "Organometallic Halide Perovskites: Sharp Optical Absorption Edge and Its Relation to Photovoltaic Performance," *The Journal of Physical Chemistry Letters* 5, no. 6 (2014): 1035–1039, https://doi.org/10.1021/jz500279b.

5. Z. Song, C. L. McElvany, A. B. Phillips, et al., "A Technoeconomic Analysis of Perovskite Solar Module Manufacturing with Low-Cost Materials and Techniques," *Energy & Environmental Science* 10, no. 6 (2017): 1297–1305, https://doi.org/10.1039/c7ee00757d.

6. C. Zhang and N.-G. Park, "Materials and Methods for Cost-Effective Fabrication of Perovskite Photovoltaic Devices," *Communications Materials* 5, no. 1 (2024): 194, https://doi.org/10.1038/s43246-024-00636-8.

7. M. A. Green, E. D. Dunlop, M. Yoshita, et al., "Solar Cell Efficiency Tables (Version 64),"*Progress in Photovoltaics: Research and Applications* 32, no. 7 (2024): 425–441, https://doi.org/10.1002/pip.3831.

8. J. Jeong, M. Kim, J. Seo, et al., "Pseudo-Halide Anion Engineering for α-FAPbI3 Perovskite Solar Cells," *Nature* 592, no. 7854 (2021): 381–385, https://doi.org/10.1038/s41586-021-03406-5.

9. S. Tao, I. Schmidt, G. Brocks, et al., "Absolute Energy Level Positions in Tin- and Lead-Based Halide Perovskites," *Nature Communications* 10, no. 1 (2019): 2560, https://doi.org/10.1038/s41467-019-10468-7.

10. S. Li, Y. Jiang, J. Xu, et al., "High-Efficiency and Thermally Stable FACsPbI3 Perovskite Photovoltaics," *Nature* 635, no. 8037 (2024): 82–88, https://doi.org/10.1038/s41586-024-08103-7.

11. J. Lim, N.-G. Park, S. Il Seok, and M. Saliba, "All-Perovskite Tandem Solar Cells: From Fundamentals to Technological Progress,"*Energy & Environmental Science* 17 (2024): 4390–4425, https://doi.org/10.1039/d3ee03638c.

12. Q.-Q. Chu, Z. Sun, J. Hah, et al., "Progress, Challenges, and Further Trends of All Perovskites Tandem Solar Cells: A Comprehensive Review," *Materials Today* 67 (2023): 399–423, https://doi.org/10.1016/j.mattod.2023.06.002.

13. S. Mariotti, E. Köhnen, F. Scheler, et al., "Interface Engineering for High-Performance, Triple-Halide Perovskite–silicon Tandem Solar Cells," *Science* 381, no. 6653 (2023): 63–69, https://doi.org/10.1126/science.adf5872.

14. Y. A. Temitmie, M. I. Haider, D. T. Cuzzupè, et al., "Overcoming the Open-Circuit Voltage Losses in Narrow Bandgap Perovskites for All-Perovskite Tandem Solar Cells," *ACS Materials Letters* 6, no. 11 (2024): 5190–5198, https://doi.org/10.1021/acsmaterialslett.4c01699.

15. Z. Liu, R. Lin, M. Wei, et al., "All-Perovskite Tandem Solar Cells Achieving >29% Efficiency with Improved (100) Orientation in Wide-Bandgap Perovskites," *Nature Materials* 24 (2025): 252–259, https://doi.org/10.1038/s41563-024-02073-x.

16. A. F. Palmstrom, G. E. Eperon, T. Leijtens, et al., "Enabling Flexible All-Perovskite Tandem Solar Cells," *Joule* 3, no. 9 (2019): 2193–2204, https://doi.org/10.1016/j.joule.2019.05.009.

17. A. Goyal, S. McKechnie, D. Pashov, W. Tumas, M. van Schilfgaarde, and V. Stevanović, "Origin of Pronounced Nonlinear Band Gap Behavior in Lead–Tin Hybrid Perovskite Alloys," *Chemistry of Materials* 30, no. 11 (2018): 3920–3928, https://doi.org/10.1021/acs.chemmater.8b01695.

18. J. Im, C. C. Stoumpos, H. Jin, A. J. Freeman, and M. G. Kanatzidis, "Antagonism between Spin–Orbit Coupling and Steric Effects Causes Anomalous Band Gap Evolution in the Perovskite Photovoltaic Materials CH3NH3Sn1–xPbxI3," *The Journal of Physical Chemistry Letters* 6, no. 17 (2015): 3503–3509, https://doi.org/10.1021/acs.jpclett.5b01738.

19. A. Al-Ashouri, A. Magomedov, M. Roß, et al., "Conformal Monolayer Contacts with Lossless Interfaces for Perovskite Single Junction and Monolithic Tandem Solar Cells," *Energy & Environmental Science* 12, no. 11 (2019): 3356–3369, https://doi.org/10.1039/c9ee02268f.

20. S. Y. Kim, S. J. Cho, S. E. Byeon, X. He, and H. J. Yoon, "Self-Assembled Monolayers as Interface Engineering Nanomaterials in Perovskite Solar Cells," *Advanced Energy Materials* 10, no. 44 (2020): 2002606, https://doi.org/10.1002/aenm.202002606.

21. G. Qu, S. Cai, Y. Qiao, et al., "Conjugated Linker-Boosted Self-Assembled Monolayer Molecule for Inverted Perovskite Solar Cells," *Joule* 8, no. 7 (2024): 2123–2134, https://doi.org/10.1016/j.joule.2024.05.005.

22. K. Guo, H. Tang, L. Han, et al., "Self-Assembled Monolayer: Revolutionizing p-i-n Perovskite Solar Cells," *ACS Energy Letters* 10, no. 10 (2025): 4882–4910, https://doi.org/10.1021/acsenergylett.5c02024.

23. S. Jia, C. Gu, X. Zhou, et al., "Self-Assembled Monolayers for High-Performance Perovskite Solar Cells," *Advanced Functional Materials* (2025), https://doi.org/10.1002/adfm.202512747.

24. Y. Yuan, H. Li, H. Luo, et al., "A Comprehensive Review of Self-Assembled Monolayers as Hole-Transport Layers in Inverted Perovskite Solar Cells," *Energies* 18, no. 10 (2025): 2577, https://doi.org/10.3390/en18102577.

25. D. Xu, P. Wu, and H. Tan, "Self-Assembled Monolayers for Perovskite Solar Cells," *Information & Functional Materials* 1, no. 1 (2024): 2–25, https://doi.org/10.1002/ifm2.8.

26. S. Wang, H. Guo, and Y. Wu, "Advantages and Challenges of Self-Assembled Monolayer as a Hole-Selective Contact for Perovskite Solar Cells," *Materials Futures* 2, no. 1 (2023): 012105,https://doi.org/10.1088/2752-5724/acbb5a.

27. J. Liu, M. Ozaki, S. Yakumaru, et al., "Lead-Free Solar Cells Based on Tin Halide Perovskite Films with High Coverage and Improved Aggregation," *Angewandte Chemie International Edition* 57, no. 40 (2018): 13221–13225, https://doi.org/10.1002/anie.201808385.

28. S. Hu, J. A. Smith, H. J. Snaith, and A. Wakamiya, "Prospects for Tin-Containing Halide Perovskite Photovoltaics," *Precision Chemistry* 1, no. 2 (2023): 69–82, https://doi.org/10.1021/prechem.3c00018.

29. Y. Zhang, C. Li, H. Zhao, et al., "Synchronized Crystallization in Tin-Lead Perovskite Solar Cells," *Nature Communications* 15, no. 1 (2024), https://doi.org/10.1038/s41467-024-51361-2.

30. L. Huerta Hernandez, M. A. Haque, A. Sharma, et al., "The Role of A-Site Composition in the Photostability of Tin–lead Perovskite Solar Cells," *Sustainable Energy & Fuels* 6, no. 20 (2022): 4605–4613, https://doi.org/10.1039/d2se00663d.

31. J. Song, T. Kong, Y. Zhang, X. Liu, M. Saliba, and D. Bi, "Synergistic Effect of Sodium Cyanoborohydride in Pb-Sn Perovskite Solar Cells," *Advanced Functional Materials* 33, no. 51 (2023), https://doi.org/10.1002/adfm.202304201.

32. S. Olthof and K. Meerholz, "Substrate-Dependent Electronic Structure and Film Formation of MAPbI3 Perovskites," *Scientific Reports* 7, no. 1 (2017), https://doi.org/10.1038/srep40267.

33. P. Schulz, E. Edri, S. Kirmayer, G. Hodes, D. Cahen, and A. Kahn, "Interface Energetics in Organo-Metal Halide Perovskite-Based Photovoltaic Cells," *Energy & Environmental Science* 7, no. 4 (2014), https://doi.org/10.1039/c4ee00168k.

34. Z. Li, Q. Tan, G. Chen, et al., "Simple and Robust Phenoxazine Phosphonic Acid Molecules as Self-Assembled Hole Selective Contacts for High-Performance Inverted Perovskite Solar Cells," *Nanoscale* 15, no. 4 (2023): 1676–1686, https://doi.org/10.1039/d2nr05677a.

35. A. Ullah, K. H. Park, H. D. Nguyen, et al., "Novel Phenothiazine-Based Self-Assembled Monolayer as a Hole Selective Contact for Highly Efficient and Stable p-i-n Perovskite Solar Cells," *Advanced Energy Materials* 12, no. 2 (2021), https://doi.org/10.1002/aenm.202103175.

36. W. S. Yang, B.-W. Park, E. H. Jung, et al., "Iodide Management in Formamidinium-Lead-Halide–based Perovskite Layers for Efficient Solar Cells," *Science* 356, no. 6345 (2017): 1376–1379, https://doi.org/10.1126/science.aan2301.

37. S. Zhang, F. Ye, X. Wang, et al., "Minimizing Buried Interfacial Defects for Efficient Inverted Perovskite Solar Cells," *Science* 380, no. 6643 (2023): 404–409, https://doi.org/10.1126/science.adg3755.

38. S. Hu, J. Pascual, W. Liu, et al., "A Universal Surface Treatment for p–i–n Perovskite Solar Cells," *ACS Applied Materials & Interfaces* 14, no. 50 (2022): 56290–56297, https://doi.org/10.1021/acsami.2c15989.

39. S. Hu, K. Otsuka, R. Murdey, et al., "Optimized Carrier Extraction at Interfaces for 23.6% Efficient Tin–lead Perovskite Solar Cells," *Energy & Environmental Science* 15 (2022): 2096–2107, https://doi.org/10.1039/d2ee00288d.

40. G. Kapil, T. Bessho, T. Maekawa, et al., "Tin-Lead Perovskite Fabricated via Ethylenediamine Interlayer Guides to the Solar Cell Efficiency of 21.74%," *Advanced Energy Materials* 11, no. 25 (2021), https://doi.org/10.1002/aenm.202101069.

41. M. I. Haider, H. Hu, T. Seewald, et al., "Ethylenediamine Vapors-Assisted Surface Passivation of Perovskite Films for Efficient Inverted Solar Cells," *Solar RRL* 7, no. 9 (2023), https://doi.org/10.1002/solr.202201092.

42. D. T. Cuzzupè, S. D. Öz, J. Ling, et al., "Understanding the Methylammonium Chloride-Assisted Crystallization for Improved Performance of Lead-Free Tin Perovskite Solar Cells," *Solar RRL* 7, no. 24 (2023), https://doi.org/10.1002/solr.202300770.

43. I. Levine, A. Al-Ashouri, A. Musiienko, et al., "Charge Transfer Rates and Electron Trapping at Buried Interfaces of Perovskite Solar Cells," *Joule* 5, no. 11 (2021): 2915–2933, https://doi.org/10.1016/j.joule.2021.07.016.

44. G. Nasti, M. H. Aldamasy, M. A. Flatken, et al., "Pyridine Controlled Tin Perovskite Crystallization," *ACS Energy Letters* 7, no. 10 (2022): 3197–3203, https://doi.org/10.1021/acsenergylett.2c01749.

45. Y. Rosenwaks, A. J. Nozik, and I. Yavneh, "The Effect of Electric Fields on Time-Resolved Photoluminescence Spectra in Semiconductors," *Journal of Applied Physics* 75, no. 8 (1994): 4255–4257, https://doi.org/10.1063/1.355964.

46. N. Drigo, C. Roldan-Carmona, M. Franckevičius, et al., "Doped but Stable: Spirobisacridine Hole Transporting Materials for Hysteresis-Free and Stable Perovskite Solar Cells," *Journal of the American Chemical Society* 142, no. 4 (2019): 1792–1800, https://doi.org/10.1021/jacs.9b07166.

47. R. A. Belisle, W. H. Nguyen, A. R. Bowring, et al., "Interpretation of Inverted Photocurrent Transients in Organic Lead Halide Perovskite Solar Cells: Proof of the Field Screening by Mobile Ions and Determination of the Space Charge Layer Widths," *Energy & Environmental Science* 10, no. 1 (2017): 192–204, https://doi.org/10.1039/c6ee02914k.

48. T. Dittrich and S. Fengler, *Surface Photovoltage Analysis of Photoactive Materials* (World Scientific, 2020), https://doi.org/10.1142/q0227.

Supporting Information

Additional supporting information can be found online in the Supporting Information section. **Supporting Fig. S1:** Synthesis of the phenoxazine and phenothiazine-based SAMs with varying length of the aliphatic linker. **Supporting Fig. S1:** Ionization energy determination of the PbSn perovskite and the SAMs via photoelectron spectroscopy in air (PESA)un. The ground level was fitted with a straight line parallel to the x axis, whereas the rising part was fitted with a straight line via linear regression. All SAMs were deposited on ITO-coated glass. **Supporting Fig. S2:** (a) UB3LYP/Def2-SVP optimized structures and their corresponding (b) HOMO and (c) LUMO of the SAMs. The orbitals were plotted at 0.036 isosurface value and the orbital energies are given in eV. **Supporting Fig. S3:** (a) UB3LYP/Def2-SVP optimized structures and their corresponding (b) HOMO and (c) LUMO of the SAMs. The orbitals were plotted at 0.036 isosurface value and the orbital energies are given in eV. **Supporting Fig. S4:** Box plots displaying the photovoltaic parameters extracted from the *J*–*V* curves for many identically processed PSC devices employing 5 different SAMs as their HTLs. For each parameter, the median valued is displayed in the middle of the box. For these datasets, no passivation was used. Device architecture: ITO/SAM/PbSn/C_{60}/BCP/Ag. **Supporting Fig. S5:** Box plots displaying the photovoltaic parameters extracted from the *J*–*V* curves for many PSC devices employing either 2PAPOz or 2PAPTz SAMs as their HTLs, without (NP: nonpassivated) and with EDA passivation (EDA), Clearly, the V_{OC} and PCE of the EDA passivated devices improves. The magnitude of the improvement is approximately the same for 2PAPOz and 2PAPTz. Device architecture: ITO/SAM/PbSn/EDA/C_{60}/BCP/Ag. **Supporting Fig. S6:** Top-view SEM images of SnPb perovskite thin films deposited on SAM-coated ITO substrates. The differences in coverage homogeneity and grain sizes are negligible or within typical sample-to-sample variations, confirming that the morphology of all samples is comparable. In other words, the grain growth is not directly influenced by the underlying SAM. **Supporting Fig. S7:** Steady-state photoluminescence spectra of PbSn perovskite deposited on SAM coated ITO substrates. The shifts in peak positions and intensities are negligible or within typical sample-to-sample variations, confirming that all photoluminescence spectra are comparable. The optical bandgap determined on the basis of this dataset is 1.25 ± 0.01 eV. **Supporting Fig. S8:** XRD diffractograms of PbSn perovskite thin films deposited on SAM-coated ITO substrates. The two primary perovskite peaks at $2\theta = 14.1°$ and $2\theta = 28.3°$, corresponding to the (100) and (200) planes, are indicated. The shifts in peak positions and intensities are negligible or within typical sample-to-sample variations, confirming that all diffractograms are comparable for this analysis.